

# Photo-Doping of Spiro-OMeTAD for Highly Stable and Efficient Perovskite Solar Cells

Seul-Gi Kim<sup>1,4,6</sup>, George C. Fish<sup>2,6</sup>, Etienne Socié<sup>2,6</sup>, Aaron T. Terpstra<sup>2,6</sup>, Dong-Am Park<sup>4</sup>, Kai Zhu<sup>1\*</sup>, Michael Grätzel<sup>3\*</sup>, Jacques-E. Moser<sup>2\*</sup> and Nam-Gyu Park<sup>4,5,7\*</sup>

<sup>1</sup>Chemistry and Nanoscience Center, National Renewable Energy Laboratory, Golden, CO 80401, USA

<sup>2</sup>Photochemical Dynamics Group, Institute of Chemical Sciences and Engineering, École polytechnique fédérale de Lausanne (EPFL); CH-1015 Lausanne, Switzerland

<sup>3</sup>Laboratory of Photonics and Interfaces, Institute of Chemical Sciences and Engineering, École polytechnique fédérale de Lausanne (EPFL); CH-1015 Lausanne, Switzerland

<sup>4</sup>School of Chemical Engineering and Center for Antibonding Regulated Crystals, Sungkyunkwan University (SKKU); Suwon 16419, Republic of Korea

<sup>5</sup>SKKU Institute of Energy Science and Technology (SIEST), Sungkyunkwan University; Suwon 16419, Republic of Korea

<sup>6</sup>These authors contributed equally.

<sup>7</sup>Lead contact.

\*Correspondence: [kai.zhu@nrel.gov](mailto:kai.zhu@nrel.gov) (K.Z), [michael.gratzel@epfl.ch](mailto:michael.gratzel@epfl.ch) (M.G), [je.moser@epfl.ch](mailto:je.moser@epfl.ch) (J.M), [npark@skku.edu](mailto:npark@skku.edu) (N.-G.P)

## SUMMARY

A widely used component of high-efficiency perovskite solar cells (PSCs) is the molecular hole-transport material (HTM) spiro-OMeTAD. This organic solid needs to be p-doped to acquire sufficient hole conductivity. However, the conventional doping method using LiTFSI in the air is slow, sensitive to the environment, and may lead to the deterioration of the PSCs by unintended oxidation or dopant migration. It is thus highly desirable to develop fast doping approaches that avoid exposing the PSC to ambient air and easy-to-move dopant ions. We report here that light absorption by spiro-OMeTAD itself triggers redox photochemistry that has so far been ignored. Strikingly, we found that Y(III) or La(III)-tBP complexes catalyze the symmetry-breaking charge separation of photo-excited spiro-OMeTAD resulting in the efficient p-doping of the HTM. Using this photo redox process, we realize PSCs with superior stability over cells using conventional doping that shows no degradation under continuous illumination over 1000 hours.

### Context & Scale

2,2',7,7'-tetrakis(N,N-di(4-methoxyphenyl)amine)-9,9'-spirobifluorene (spiro-OMeTAD) as a molecular hole-transport material (HTM) has been used for high-efficient n-i-p structured perovskite solar cells (PSCs). This organic HTM needs to be p-doped to acquire a sufficient hole conductivity. The conventional doping method using lithium bis(trifluoromethane)sulfonimide (LiTFSI) takes long time (~days) and shows low operational stability in PSCs.

Here, we discovered redox photochemistry of spiro-OMeTAD itself and photo-redox doping process by the symmetry-breaking charge separation which is modulated by Y(III) or La(III)-tBP complexes. Using this photo redox doping process, PSCs shows superb light-soaking stability demonstrating no degradation under continuous illumination over 1000 hours.

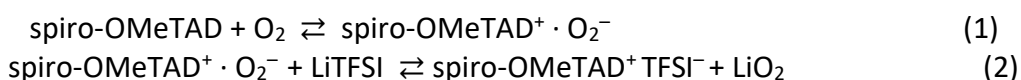
Keywords: Perovskite solar cell, Photo-redox, Photo doping, Stability, La(TFSI)<sub>3</sub>

## INTRODUCTION

Lead trihalide perovskite materials have been applied as an intrinsic absorber in next-generation photovoltaic devices based on heterojunction (n-i-p or p-i-n) structures. The power conversion efficiency (PCE) of perovskite solar cells (PSCs) is now comparable to that of

the best single-junction silicon systems. Since the advent in 2012 of solid-state methylammonium lead triiodide (MAPbI<sub>3</sub>) based PSCs, reaching power conversion efficiencies (PCEs) close to 10%,<sup>1,2</sup> a vast amount of research on organic–inorganic halide PSCs has allowed to reach currently a certified PCE of 25.8%.<sup>3</sup> The thickness of the PSC light-harvesting layer is about 300 times less than that of current Si-cells resulting in a much higher power density per unit weight. Their large open circuit photovoltage as well as the possibility of fabricating them by simple solution processing constitute other key advantages.

Today's top efficiency PSCs commonly employ a normal (n–i–p) device configuration, including TiO<sub>2</sub> or SnO<sub>2</sub> as an electron transporting material (ETM) and spiro-OMeTAD as a molecular HTM. LiTFSI and 4-tert-butylpyridine (tBP) are commonly incorporated as additives in the HTM with a typical molar ratio spiro-OMeTAD:LiTFSI:tBP of 1:0.5:3. The role of lithium cations is to promote p-doping of the HTM by excessive oxygen, leading to the formation of the spiro-OMeTAD<sup>+</sup> radical cation and lithium oxide according to Eqs 1, 2.<sup>4-6</sup>



Hence the role of the lithium cations is to scavenge the superoxide anions formed during the oxidation of the HTM by excessive oxygen which shifts the equilibrium to the product side. On the other hand, tBP increases the solubility of the lithium salts in chlorobenzene (CB) which serves as a solvent for the hole conductor. Both LiTFSI and tBP additives clearly have a beneficial effect on the photovoltaic performances of PSCs, albeit at the cost of impaired device stability. A caveat of this conventional aging process is that it takes a few days after device fabrication depending on the environment. Most industrial dry air generators (compressed or refrigerated systems) could provide dry air that has a dew point of -30~-60 °C (450~15 ppm of H<sub>2</sub>O exists). Mixed gas is not preferred in terms of cost-effectiveness. Many experiments reported elsewhere were conducted in dry air, said RH < 1% condition, which contains, however, ~300 ppm of H<sub>2</sub>O. In this RH < 1% condition, the aging process could be shortened by about ~24~36 hours compared to the dry air condition with H<sub>2</sub>O < 0.1 ppm,<sup>4</sup> albeit at the cost of the impaired spiro-OMeTAD layer (Figure S1).<sup>7</sup> Also, the extent of doping is ill-controlled and the process may entail degradation of the perovskite layer by unintentional oxidation or exposure to moisture.<sup>8-11</sup> In addition, the presence of Li<sup>+</sup> ions could jeopardize device stability as they are prone to migration under the electric field that is present across the device under light illumination.<sup>12</sup>

Alternative doping materials for spiro-OMeTAD have been studied to replace Li additive as a way to avoid the post-oxidation process and to improve stability. The perfluoro-tetracyanoquinodimethane (F4TCNQ), tris-(pentafluorophenyl)borane and benzoyl peroxide were found to oxidize spiro-OMeTAD.<sup>13-16</sup> Also, directly mixing with synthesized spiro-OMeTAD<sup>+</sup> radical salt (spiro-TFSI) was studied.<sup>17</sup> However, those studies showed low device performance. Very recently, the use of organic radical ionic salts (4-tert-butyl-1-methylpyridinium bis(trifluoromethylsulfonyl)imide (TBMP<sup>+</sup>TFSI<sup>-</sup>) allowing for 25% of PCE and

humidity stability were reported.<sup>18</sup> Several other metal cation dopants also have been proposed as a replacement for LiTFSI.<sup>19</sup> (Tris(2-(1H-pyrazol-1-yl)-4-tert-butylpyridine) cobalt(III) tri[bis(trifluoromethane)sulfonimide] (FK209) is used as co-additive in presence of LiTFSI.<sup>20</sup> The Ca<sup>2+</sup> and Mg<sup>2+</sup> were also investigated. However, these dopants require an aging process.<sup>21</sup> The PSCs with Cu<sup>2+</sup> or Mo<sup>6+</sup> showed low efficiency (13.4–16.7%).<sup>22, 23</sup> Zn<sup>2+</sup> additive showed stable operation for 600 h with 17.3% of PCE.<sup>24,25</sup> However, this needs the co-additive FK209 to improve PCE to 21.3%. In Table S1, doping materials for spiro-OMeTAD and the resulting conductivities are summarized.

We report here that light absorption by spiro-OMeTAD itself triggers redox photochemistry that has so far been ignored. Strikingly, we find that group IIIb metal cations-tBP complexes, in particular Y<sup>3+</sup>-tBP and La<sup>3+</sup>-tBP complexes, catalyze the fast quenching of photo-excited spiro-OMeTAD molecules through a light-induced symmetry-breaking charge separation process. Further oxidation of spiro anions by oxidizer traces yields remaining oxidized spiro-OMeTAD<sup>+</sup> cations, affording efficient p-doping of the HTM, which enabled >24%-efficient PSCs with no degradation under 1-sun operation over 1000 h.

## RESULTS AND DISCUSSION

### Photo-doping of spiro-OMeTAD in the presence of metal-tBP complexes

The absorption spectrum of the spiro-OMeTAD solution shows an onset at 420 nm, and the addition of tBP and TFSI<sup>-</sup> anions in the form of various metal cation salts did not affect these spectra (Figure S2). Continuous irradiation of these deoxygenated solutions by a white LED in an N<sub>2</sub> glove box with a trace of oxygen environment produced a change in their appearance from colorless to magenta (**Figure 1A**). UV-vis spectra show that the appearance of the magenta coloring corresponds to the growth of a new absorption band peaking at 525 nm and displaying a pronounced shoulder around 485 nm (**Figure 1B**). As this feature is unambiguously assigned to the oxidized spiro-OMeTAD<sup>+</sup> radical cations,<sup>26</sup> this shows that electron abstraction from the spiro-bifluorene derivative takes place upon irradiation with wavelengths  $\lambda_{\text{exc}} \leq 420$  nm<sup>27</sup> (Figures S3-S4) not by the heat (Figure S5). The efficiency of the photo-oxidation gradually increases as the charge carried by metal cations increases from +1 to +3. Furthermore, it seems to slightly decrease when the period of the element increases, i.e. Li<sup>+</sup> > Na<sup>+</sup> > K<sup>+</sup>  $\approx$  Rb<sup>+</sup>  $\approx$  Cs<sup>+</sup>, Mg<sup>2+</sup> > Ca<sup>2+</sup> > Sr<sup>2+</sup>  $\approx$  Ba<sup>2+</sup> and Sc<sup>3+</sup> > Y<sup>3+</sup>  $\approx$  La<sup>3+</sup>.

### Photochemistry of spiro-OMeTAD with M<sup>3+</sup>-tBP complex

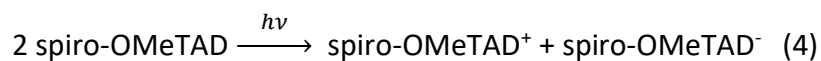
To figure out the enhanced photooxidation of spiro-OMeTAD in the presence of Y<sup>3+</sup>- and La<sup>3+</sup>-tBP complexes, optoelectronic analyses were carried out in an inert condition. The fluorescence spectrum of spiro-OMeTAD solution in CB is characterized by negligible Stokes' shift and peaks at 445 nm with no apparent shoulder (Figure S6). Fast fluorescence lifetimes of spiro-OMeTAD in solution were evaluated to  $\tau = 2.21 \pm 0.01$  ns (for neat spiro-OMeTAD),  $2.0 \pm 0.1$  ns (with Li<sup>+</sup>-tBP),  $1.8 \pm 0.1$  ns (with Y<sup>3+</sup>-tBP), and  $1.6 \pm 0.1$  ns (with La<sup>3+</sup>-tBP) by time-correlated single photon counting (TCSPC) (Figure S7). This shortening of the fluorescence lifetime denotes the quenching of the spiro-OMeTAD excited states by the additives. Quantum yields of the quenching process ( $\Phi_q$ ) can be evaluated using Eq. 3, where  $\tau_0$  and  $\tau_q$  are the

fluorescence lifetimes in the absence and presence of a quencher.  $\Phi_q$  values of  $9 \pm 5\%$ ,  $18 \pm 4\%$ , and  $28 \pm 5\%$  were calculated for  $\text{Li}^+$ -tBP,  $\text{Y}^{3+}$ -tBP and  $\text{La}^{3+}$ -tBP additives, respectively.

$$\Phi_q = 1 - \left( \tau_q / \tau_0 \right) \quad (3)$$

The emission lifetime in films was also evaluated by fluorescence up-conversion spectroscopy (FLUPS, time resolution  $< 200 \text{ fs}^{28}$ ) as the fluorescence decay in films appears to be 2~3 orders of magnitude faster than in solutions. (Figures S8-S9). Additional quenching of the fluorescence in the presence of  $\text{La}^{3+}$  ion, in the absence and presence of tBP, was studied by comparing the temporal profiles of spiro-OMeTAD emission. A biexponential decay of the fluorescence of neat spiro-OMeTAD film shows  $\tau_1 = 2.6 \text{ ps}$  ( $\sim 50\%$ ) and  $\tau_2 = 14.5 \text{ ps}$  ( $\sim 50\%$ ) which are similar to those observed with tBP (**Figure 2A**). In the presence both of the  $\text{La}^{3+}$  and tBP, the slow decay component disappears, and the emission lifetime is reduced to  $\tau_q = 2.6 \text{ ps}$  (**Figure 2B**). The  $\Phi_q$  of the spiro-OMeTAD film with  $\text{La}^{3+}$  and tBP was evaluated to 82%, where  $\tau_0 = 14.5 \text{ ps}$  and  $\tau_q = 2.6 \text{ ps}$ . This exceeds markedly the 18% molar ratio of  $\text{La}^{3+}$  to spiro-OMeTAD indicating that the  $\text{La}^{3+}$  cations may be dispersed in the film in such a way that each cation is in close vicinity with five to six spiro-OMeTAD molecules, allowing for the photo-doping reaction which proceeds within a few picoseconds. Importantly, the quenching of the slow fluorescence decay component is not observed in the absence of tBP, indicating that the presence of both tBP and  $\text{M}^{3+}(\text{TFSI})_3$  is required for the very rapid quenching of spiro-OMeTAD excited states. The formation of metal-tBP complexes, especially,  $\text{Y}^{3+}$ - and  $\text{La}^{3+}$ - tBP complexes, was confirmed by FTIR, H-NMR, UV-Vis and DFT calculation (Figures S10-S13, Table S2 and Notes S1-S2).

Femtosecond transient absorption (TA) spectroscopy was used to unravel the quenching mechanism of spiro-OMeTAD electronic excited states in the presence of  $\text{M}^{3+}$ -tBP complexes in the film. As shown in **Figure 2C-D**, the TA spectra of the spiro-OMeTAD film with only tBP or with  $\text{La}^{3+}$ -tBP complex similarly display a broad positive feature between 450 and 650 nm. A global analysis procedure was applied to disentangle the different spectral components in the transient spectra, as well as provide information on the lifetimes of the photogenerated species. In the decay-associated spectra (DAS) yielded from TA spectra (**Figure 2E-F**), the absorption band with a characteristic peak at 525 nm is assigned to the spiro-OMeTAD<sup>+</sup> oxidized species and a broad absorption band with 575 nm peak is assigned to the excited state of the spiro-OMeTAD\*. In spiro-OMeTAD films with only tBP (**Figure 2E**), the reaction yielding the oxidized radical cation is characterized by a time constant of 17 ps. The absence of any oxidizer to the system infers that spiro-OMeTAD<sup>+</sup> can only be photo-generated along with spiro-OMeTAD<sup>-</sup> reduced anion by a symmetry-breaking photoinduced charge separation process (Eq. 4).<sup>29, 30</sup> However, the time constant of this reaction markedly reduces to 2.6 ps after addition of  $\text{La}^{3+}$ -tBP (**Figure 2F**), in good agreement with the values extracted from FLUPS experiments.



The time constant of the oxidized species decays through a back electron transfer process in the spiro-OMeTAD film with only tBP is 560 ps (**Figure 2E**). In the presence of  $\text{La}^{3+}$ -tBP complex, a time constant of spiro-OMeTAD<sup>+</sup> oxidized cation is reduced to 94 ps (**Figure 2F**). This kinetics is independent of the pump energy fluence (Figure S14) which can be concluded that the oxidized species undergoes geminate recombination with the reduced products (Eq. 5).



The presence or absence of only tBP or the addition of  $\text{La}(\text{TFSI})_3$  in the film deprived of tBP has no effect on the dynamics of the spiro-OMeTAD excited state. Strikingly, the spiro-OMeTAD with LiTFSI (w/o tBP) shows an absorption feature with a maximum at 525 nm, whose lifetime extends beyond 1 ns (Figure S15). This shows that a photochemical reaction appears to occur in spiro-OMeTAD with LiTFSI even in the absence of tBP. However, its long lifetime is in variance with that measured with  $\text{La}(\text{TFSI})_3$  and tBP, excluding fast recombination with a reduced spiro anion. Therefore, FLUPS and TA measurements confirmed that  $\text{La}^{3+}$ -tBP complex catalyzes the symmetry-breaking photoinduced charge separation in spiro-OMeTAD film, and this symmetry-breaking mechanism does not apparently take place in the presence of LiTFSI-based spiro-OMeTAD.

### Photo doping mechanism

**Figure 3** provides an energetic scheme of the electron transfer reactions leading to the photo-doping of spiro-OMeTAD by irradiation at wavelengths  $\leq 420$  nm. We posit that the primary photoinduced charge separation takes place according to Eq. 4 as a rate-determining step. In a homogeneous environment, photoinduced charge separation within a symmetric spiro-OMeTAD molecular pair (dotted black arrow) is hindered by the Laporte rule and lack of thermodynamic driving force. Indeed, without  $\text{La}^{3+}$ -tBP or  $\text{Y}^{3+}$ -tBP complexes, a large portion of excited species are relaxed to the ground state by emitting fluorescence. The interaction of one of the molecules ( $S_B$ ) with a neighboring  $M^{3+}$ -tBP complex affects its energetics and causes explicit symmetry-breaking that would lead to a small shift of the HOMO and LUMO energy levels of the  $S_B$ . This effect is apparently strongly increased by the proximity of  $\text{Y}^{3+}$ - or  $\text{La}^{3+}$ -tBP complexes which leads to fast initial kinetics (Figure S16) and concentration dependence of the  $M^{3+}$ -tBP complex (Figure S17) in photo doping reaction. As a result, ultrafast electron transfer (step 2) can take place from the excited state of  $S_A$  to  $S_B$  (oxidative quenching of  $S_A^*$ , left) or from  $S_A$  ground state to the excited state of  $S_B$  (reductive quenching of  $S_B^*$ , right). Kinetic competition between charge recombination (step 3) and electron transfer from the reduced spiro-OMeTAD anions ( $S_B^-$ ) to oxidizer traces (step 4), such as  $\text{O}_2$  dissolved in the organic matrix (Figure S18), determines the concentration of remaining oxidized spiro-OMeTAD cations ( $S_A^+$ ) that ensures the final p-doping of the hole transport material and a strong increase of the hole conductivity.

### Characteristics of photo-doped spiro-OMeTAD and photovoltaic performance

Conductivities ( $\sigma$ ) of photo-doped spiro-OMeTAD employing representative metal-tBP complexes according to their charges ( $\text{Li}^+$ ,  $\text{Rb}^+$ ,  $\text{Sr}^{2+}$ ,  $\text{Y}^{3+}$  and  $\text{La}^{3+}$ ) (Figure S19 and Table S3) and

depending on the concentration of  $\text{La}^{3+}$  (Figure S20 and Table S4) were evaluated. The  $\sigma$  is enhanced as the group of the metal ion increases from  $\text{M}^{\text{I}}$  to  $\text{M}^{\text{III}}$ , (i.e.  $\sigma$  ( $\Omega \cdot \text{cm}$ ) $^{-1}$  =  $1.35 \times 10^{-8}$  ( $\text{Rb}^+$ ),  $8.02 \times 10^{-7}$  ( $\text{Sr}^{2+}$ ),  $5.90 \times 10^{-5}$  ( $\text{Y}^{3+}$ ) and  $6.06 \times 10^{-5}$  ( $\text{La}^{3+}$ )), where  $\text{La}^{3+}$  system shows an optimized conductivity when the molar ratio of  $[\text{La}^{3+}]/[\text{spiro}]$  approaches 0.18, even higher than LiTFSI-based spiro-OMeTAD after conventional dry air aging ( $7.87 \times 10^{-6}$  (72 h) and  $1.34 \times 10^{-5}$  (168 h)). Here, we used dry air ( $\text{H}_2\text{O} < 0.1$  ppm) for the conventional air aging process. The  $\sigma$  of both photo-doped ( $\text{La}^{3+}$ ) and conventional dry-air-aged ( $\text{Li}^+$ ) spiro-OMeTAD layer was well maintained in the dark storage condition after a slight decrease in the  $\sigma$  during the first 60 hours (Figure S21). UV-Vis spectra of the photo-doped products with  $\text{La}^{3+}$ -tBP complex (both solution and film) were compared with the mixture of spiro-OMeTAD and spiro(TFSI) to find an oxidative conversion efficiency in the photo-doping process. It is detected that 0.4% of spiro-OMeTAD was converted to spiro-OMeTAD $^+$  in solution after the photo-doping process (Figure S22). In film, the conversion yield is more enhanced to 2.8% (Figure S23). Similar to the solution, this conversion occurs rapidly in the first few minutes and reaches equilibrium after 30 minutes of the photo-doping process. The conductivity of the film, accordingly, no longer exhibits a significant increase beyond the initial 30 minutes (Figure S24 and Table S5). Also, the signal of  $\text{La}^{3+}$ -tBP complex ( $\lambda < 440$  nm, Figure S12) in the film is more pronounced compared to the solution (Figure S2) as shown in Figure S25.

The charge extraction ability from perovskite to photo-doped spiro-OMeTAD were also evaluated by steady-state photoluminescence (PL) and time-resolved PL (TRPL) $^{31}$  (Figure 4A-B and Table S6). Decrement in PL intensity and average carrier lifetime ( $\tau_{\text{av}}$ ) of  $\text{Y}^{3+}$ - and  $\text{La}^{3+}$ -tBP complex-based device ( $\tau_{\text{av}}$  (ns) = 4.18 ( $\text{Y}^{3+}$ ) and 3.96 ( $\text{La}^{3+}$ )) indicates better charge extraction efficiency, which is due to the enhanced conductivity and better interface. Improved charge extraction efficiency is confirmed by the transient photo-voltage (TPV) and transient photo-current (TPC) measurements (Figure S26 and Note S3). This contributes to higher  $J_{\text{sc}}$  and FF for the PSCs employing the photo-doped spiro-OMeTAD with  $\text{Y}^{3+}$ - and  $\text{La}^{3+}$ -tBP complex.

Ultraviolet photoelectron spectroscopy (UPS) shows that the valence band energies ( $E_{\text{VB}}$ s) of photo-doped spiro-OMeTAD (-6.10 eV for  $\text{Y}^{3+}$ -tBP and -6.27 eV for  $\text{La}^{3+}$ -tBP) are lower than that of  $\text{Li}^+$ -tBP-based spiro-OMeTAD (-5.81 eV, aged in dry air) (Figure 4C, Figure S27 and Note S4), leading to decrement of energy level gap ( $\Delta E_{\text{VB}}$ ) between perovskite and spiro-OMeTAD from 0.76 eV (LiTFSI) to 0.47 eV ( $\text{Y}^{3+}$ -tBP) and to 0.30 eV ( $\text{La}^{3+}$ -tBP), which contributes to reducing  $V_{\text{oc}}$  loss in PSCs. $^{32-34}$  Therefore, PSCs employing  $\text{Y}^{3+}$ - and  $\text{La}^{3+}$ -tBP complexes-based photo-doped spiro-OMeTAD show enhanced PCEs (24.00% for  $\text{Y}^{3+}$  and 24.13% for  $\text{La}^{3+}$ ) with noticeable improvements in  $V_{\text{oc}}$  and FF and a slight increment in  $J_{\text{sc}}$  (Figure S28) compared to 23.06% for the air-oxidized  $\text{Li}^+$ -tBP based spiro-OMeTAD (Figure 4D-F). A schematic illustration of the device fabrication process including the photo-doping procedure is presented to compare the conventional fabrication process (Figure S29). For photovoltaic performance of other metal-tBP complexes-based photo-doped PSCs, see Figures S30-S32 and Note S5. In addition, a similar improvement in photovoltaic performance is observed when  $\text{Y}^{3+}$ - and  $\text{La}^{3+}$ -tBP are applied to different perovskite composition, such as  $\text{FAPbI}_3$  (Figure S33). Since the co-additive FK209 was reported to show better stability and efficiency than the spiro-OMeTAD without FK209, $^{24}$  we added FK209 in the photo-doping system with  $\text{La}^{3+}$ -tBP complex.

However, the photovoltaic performance was rather deteriorated due to the decreased  $V_{oc}$  (Figure S34).

### Long-term stability

A fast and significant degradation during the first 100 h operation (often referred to as “burn-in”) is frequently observed in n-i-p devices.<sup>35, 36</sup> This undesirable burn-in effect associated with ion migration in PSCs will result in charge barriers with accumulated ions and vacancies at interfaces.<sup>37,38</sup> Given that the perovskite layer is permeable to  $Li^+$  ions<sup>39</sup>, the migration of  $Li^+$  ions is often a main factor of degradation in the early stage of PSC operation.<sup>40</sup> The accumulated ions could trigger destructive reactions at the perovskite/HTM interfaces during long-term device operation.<sup>41</sup> Moreover, lithium ion in the perovskite layer causes degradation of the perovskite phase and deterioration of photovoltaic performance.<sup>12,42,43</sup>

Contrary to the substantial accumulation of lithium ion at perovskite/ $SnO_2$  interface as a consequence of its migration from spiro-OMeTAD (**Figure 5A**), the  $Y^{3+}$  and  $La^{3+}$  ions in the photo-doped spiro-OMeTAD are hardly diffused into perovskite layer even after maximum power point tracking (MPPT) for 1008 hours under illumination (ISOS-L-1I<sup>44</sup>) (**Figure 5B-C**). Inhibition of ion migration and accumulation contributes to preventing the degradation of the perovskite surface (Figure S35). PCE of the PSCs employing photo-doped spiro-OMeTAD with  $Y^{3+}$ - or  $La^{3+}$ -tBP complexes was also tracked during the illumination stability test and compared to conventionally doped LiTFSI-based PSCs (**Figure 5D** and Figures S36-S37). Devices for stability test show an initial PCE ( $PCE_0$ ) of 21.9% ( $Li^+$ -tBP), 22.3% ( $Y^{3+}$ -tBP) and 22.5% ( $La^{3+}$ -tBP), where we used a relatively low transparent FTO substrate (Figure S38). Almost no degradation is observed for  $Y^{3+}$ - and  $La^{3+}$ -tBP based PSCs ( $PCE_{1008}/PCE_0 = 1.008$  for  $Y^{3+}$ -tBP and 0.999 for  $La^{3+}$ -tBP) for 1008 hours along with no “burn-in” behavior, whereas the LiTFSI based PSCs show “burn-in” in the first 60 hour-operation as well as continuous degradation during the light soaking test ( $PCE_{1008}/PCE_0 = 0.802$ ).

A pronounced thermal storage stability at 85 °C (in the dark) over 1000 hours (ISOS-D-2I<sup>44</sup>) is observed at the same time for the devices with  $Y^{3+}$ - and  $La^{3+}$ -tBP-based spiro-OMeTAD, which is due to less lowered glass transition temperature ( $T_g$ ) of pristine spiro-OMeTAD after additive addition (85.3 °C for  $Y^{3+}$  and 85.2 °C for  $La^{3+}$  versus 95.4 °C for pristine spiro-OMeTAD) than the  $Li^+$ -tBP case (70.7 °C) (Figure S39). Stronger electrostatic interaction between trivalent ion ( $Y^{3+}$  and  $La^{3+}$ ) and both tBP and spiro-OMeTAD matrix might inhibit the deformation of the spiro-OMeTAD layer under thermal stress (Figure S40) and suppress the diffusion of  $Y^{3+}$  and  $La^{3+}$  ion into the perovskite layer (Figure S41).

The  $Y^{3+}$ - and  $La^{3+}$ -tBP-based PSCs maintain 67.3% and 62.9% of  $PCE_0$ , respectively, whereas the  $Li^+$ -tBP-based one maintains merely 14.9% of its  $PCE_0$  after 1032 hour-thermal stress at 85 °C in the dark (Figure S42). An operational stability test at an elevated temperature of 65 °C under illumination was also conducted (Figure S42), where much better stability is observed for the  $Y^{3+}$ - and  $La^{3+}$ -tBP-based PSCs (92.4% of  $PCE_0$  for  $Y^{3+}$  and 92.2% of  $PCE_0$  for  $La^{3+}$  are maintained after 230 hours) than for the  $Li^+$ -tBP-based one (73.3% of  $PCE_0$ ).

## Conclusion

In conclusion, we have discovered a new p-doping process for spiro-OMeTAD, which is widely used as a solid-state hole conductor in molecular and perovskite-based photovoltaics. The p-doping involves a photo-induced redox process that is initiated by light excitation of the hole conductor itself and is strongly enhanced by the symmetry breaking of excited hole conductor molecules in the presence of  $Y^{3+}$ - or  $La^{3+}$ -tBP complexes. Using this photo-doping method, deterioration by unintended oxidation and/or moisture- and dopant-mediated degradation can be avoided since the devices do not require additional aging processes in the air. Here, we realize PSCs with far superior operational stability than conventional doping by  $Li^+$  ions. The devices show practically no degradation under full sun illumination and maximum power point tracking over 1,000 hours while maintaining excellent power conversion efficiency.

## EXPERIMENTAL PROCEDURES

### Resource Availability

#### *Lead Contact*

Further information and requests for resources should be directed to and will be fulfilled by the lead contact, Nam-Gyu Park ([npark@skku.edu](mailto:npark@skku.edu)).

#### *Materials Availability*

All unique reagents generated in this study are available on request from the lead contact without restriction.

#### *Data and Code Availability*

This study did not generate any datasets.

### Synthesis of formamidinium iodide (FAI) and 4-Fluoro Phenethylammonium iodide (4F-PEAI)

15 g of formamidinium acetate (99%, Sigma Aldrich) was reacted with 30 mL of hydroiodic acid (57 wt% in water, Sigma Aldrich) in an ice bath. After stirring for 30 min, the brown precipitate was formed by evaporating the solvent at 60 °C using a rotary evaporator. The solid precipitate was washed with diethyl ether (99.0 %, SAMCHUN) several times, which was followed by recrystallization in anhydrous ethanol. The white precipitate was filtered and dried under vacuum for 24 h, which was stored in a glove box filled with Ar. 4F-PEAI (1.39 g of 4-Fluorophenethylamine (99%, Aldrich) reacted with 1.5 mL of hydroiodic acid (57 wt% in water, Sigma Aldrich) was also synthesized and recrystallized same method with FAI.

### Synthesis of metal bis(trifluoromethanesulfonyl)imide salt (Metal-TFSI)

Metal-TFSI salts were synthesized by reacting 1 g of bis(trifluoromethanesulfonyl)imide acid (HTFSI) (>99.0 %, TCI) in 10 mL of EtOH with an equimolar amount of metal(+I) acetate (M(Ac)), M =  $Li^+$  (lithium acetate, 99.95%, Sigma Aldrich), M =  $Na^+$  (sodium acetate, 99.0%, Sigma Aldrich), M =  $K^+$  (potassium acetate, 99.0%, Sigma Aldrich), M =  $Rb^+$  (rubidium acetate, 99.8%, Alfa Aesar), M =  $Cs^+$  (cesium acetate, 99.99%, Sigma Aldrich)), with 1/2 equivalents of metal(+II)

acetate ( $M(\text{Ac})_2$ ),  $M = \text{Mg}^{2+}$  (magnesium acetate tetrahydrate, 99 %, Sigma Aldrich),  $M = \text{Ca}^{2+}$  (calcium acetate monohydrate,  $\geq 99$  %, Sigma Aldrich),  $M = \text{Sr}^{2+}$  (strontium acetate,  $\geq 99.995$  %, Sigma Aldrich),  $M = \text{Ba}^{2+}$  (barium acetate,  $\geq 99.999$  %, Sigma Aldrich) and with 1/3 equivalents of metal(+III) acetate ( $M(\text{Ac})_3$ ),  $M = \text{Sc}^{3+}$  (scandium acetate hydrate, 99.9 %, Sigma Aldrich),  $M = \text{Y}^{3+}$  (yttrium acetate hydrate, 99.95%, Sigma Aldrich),  $M = \text{La}^{3+}$  (lanthanum acetate hydrate, 99.9%, Sigma Aldrich) in 10 mL of EtOH. The reaction proceeded by mixing the solution drop by drop at temperature  $< -5$  °C and  $\text{N}_2$  condition. After stirring for 30 min, a cloudy and goopy product was formed by evaporating the solvent at 60 °C using a rotary evaporator. The product was dissolved in acetonitrile (ACN) and filtered using a PTFE filter. A white powder formed after removing the solvent in a rotary evaporator was dried in a vacuum at 150 °C for 8 h. All hydrate salts were dried in a dry oven at 110 °C for 48 h.

### Device Fabrication

The patterned fluorine-doped tin oxide (FTO) glass (TEC-7, 8  $\Omega/\text{sq}$ ) was ultrasonically cleaned with detergent, DI water, ethanol and acetone sequentially, which was further treated by ultraviolet-ozone (UVO) for 40 min to remove organic contaminants. For the best-performing devices, antireflection (AR) coated high transparent FTO (Asahi VU1.8T, 10  $\Omega/\text{sq}$ ) substrates were used. The 4 wt%  $\text{SnO}_2$  aqueous colloidal solution, obtained by diluting 15 wt%  $\text{SnO}_2$  aqueous colloidal solution (Alfa Aesar), was spin-coated on the FTO substrates at 3,000 rpm for 30 s and then annealed on a hot plate at 185 °C for 30 min in ambient air. For high-efficiency PSCs, 0.15 M quantum dot tin oxide (QD- $\text{SnO}_2$ ) suspension was used, which was prepared by stirring 1.34 g of  $\text{SnCl}_2 \cdot 2\text{H}_2\text{O}$  ( $>99.995\%$ , Sigma Aldrich) and 0.4448 g of thiourea ( $>99.999\%$ , Sigma Aldrich) in 60 ml of DI water for 96 hours in ambient air condition (RH 40~55%, 22~25 °C). After cooling down to room temperature, the film was exposed to UVO for 40 min before depositing perovskite layer. After then, substrates are transferred to LED installed  $\text{N}_2$  glove box (5 ppm of trace  $\text{O}_2$ ,  $\text{H}_2\text{O} < 0.1$  ppm).

For deposition of K-doped  $\text{FA}_{0.92}\text{Cs}_{0.08}\text{PbBr}_{0.15}\text{I}_{2.85}$  perovskite<sup>38,42</sup>, a precursor solution was prepared by dissolving, 0.0170 g of CsBr (99.999%, Sigma Aldrich), 0.0128 g of  $\text{PbBr}_2$  (99.999%, TCI), 0.1592 g of FAI and 0.4449 g of  $\text{PbI}_2$  (99.99%, TCI) in 0.50 mL *N,N'*-dimethylformamide (DMF, 99.8% anhydrous, Sigma Aldrich), 40  $\mu\text{L}$  of KI stock solution (100 mM in DMF) and 75  $\mu\text{L}$  dimethyl sulfoxide (DMSO,  $>99.5\%$ , Sigma Aldrich). The solution was prepared and filtered with a 0.2  $\mu\text{m}$  pore-sized PTFE-H filter (Hyundai MICRO) in Ar condition. Prior to coating, the precursor solutions were sealed and mildly stirred at 50 °C for 10 min in an ambient condition. The precursor solution was spin-coated on the  $\text{SnO}_2$  film at 4,000 rpm for 20 s, where 0.35 mL of diethyl ether (99.9%, Sigma Aldrich) was dripped after rotating for 10 s. The as-deposited film was heated at 150 °C for 20 min.

For interfacial engineering, 30  $\mu\text{L}$  of 10 mM 4-fluoro-phenylethylammonium iodide (4F-PEAI) solution, prepared by dissolving 0.0267 g of 4F-PEAI in 10 ml of isopropyl alcohol (IPA), was spin-coated on the annealed perovskite film at 6,000 rpm for 20 s.

20  $\mu\text{L}$  of spiro-OMeTAD solution, prepared by dissolving 72.3 mg of spiro-OMeTAD (Lumtec), 28.8  $\mu\text{L}$  of 4-*tert*-butyl pyridine (tBP) and 17.5  $\mu\text{L}$  of metal-TFSI ( $\text{M}^{\text{n}+}(\text{TFSI})_n$ ) solution ( $\text{M}^{\text{n}+} = \text{Li}^+$  (520 mg),  $\text{Na}^+$  (549 mg),  $\text{K}^+$  (578 mg),  $\text{Rb}^+$  (662 mg),  $\text{Cs}^+$  (748 mg),  $\text{Mg}^{2+}$  (529 mg),  $\text{Ca}^{2+}$  (543 mg),  $\text{Sr}^{2+}$  (586 mg),  $\text{Ba}^{2+}$  (631 mg),  $\text{Sc}^{3+}$  (534 mg),  $\text{Y}^{3+}$  (561 mg), and  $\text{La}^{3+}$  (591 mg) in 1 mL of acetonitrile (99.8%, Sigma Aldrich)) in 1 mL of chlorobenzene in an argon atmosphere, which was spin-coated on the perovskite layer at 3,000 rpm for 20 s in the glove box. Devices were photo-oxidized under white LED for 30 minutes (white LED, 1  $\text{mW cm}^{-2}$ ). The temperature was maintained under 45  $^\circ\text{C}$  during the illumination. Finally, Au (for illumination and thermal stability) or Ag (for best-performing devices) electrode was deposited by using a thermal evaporator at an evaporation rate of 0.05 nm/s at pressure  $< 8.0 \times 10^{-7}$  Torr and temperature ranging between 25  $^\circ\text{C}$  and 32  $^\circ\text{C}$  after 12h~48h in vacuum. For conventional devices with LiTFSI, PSCs were aged in dry air ( $\text{H}_2\text{O} < 0.1$  ppm, mixed gas-air ratio) for 72 h before characterization. Photo-doped devices were kept in the glove box. For photo-doped device ( $\text{La}^{3+}$ -tBP) with FK209 (Tris(2-(1H-pyrazol-1-yl)-4-*tert* butylpyridine) cobalt(III) tris(bis(trifluoromethylsulfonyl) imide)) co-additive, 3  $\mu\text{L}$  of FK209 solution (375 mg/ml in ACN) was added.

### Characterizations

UV/Vis spectra were measured on a JASCO (V-570) UV/Vis/NIR spectrophotometer and a Cary 7000 UV/Vis/NIR spectrophotometer. The fluorescence spectra of solutions were recorded using a JASCO FP 6200 spectrometer. The concentration of solutions for UV-Vis was  $2.95 \times 10^{-2}$  M (spiro-OMeTAD) in CB. The molar ratio of spiro-OMeTAD/tBP/metal ion was 1/3.34/0.54 ( $\text{Li}^+ \sim \text{Cs}^+$ ), 0.36 ( $\text{Mg}^{2+} \sim \text{Ba}^{2+}$ ) and 0.18 ( $\text{Sc}^{3+} \sim \text{La}^{3+}$ ). Spiro(TFSI) was synthesized by reacting spiro-OMeTAD and AgTFSI 1:1 molar ratio with DCM solvent in  $\text{N}_2$ . Then, dark powder was collected after filtering and evaporating the solvent. Spiro(TFSI) was washed with diethyl ether. UV-curable epoxy was used for encapsulation.

Fluorescence spectra of solid films were acquired on a spectrofluorometer instrument (Fluorolog-3, Horiba Jobin Yvon) by exciting the samples at a fixed wavelength of 350 nm. Time-correlated single photon counting (TCSPC) measurements were carried out with the same instrument by using a 350 nm pulsed light-emitting diode (nanoLED, Horiba) as an excitation source ( $\sim 500$  ps pulse length, 100 kHz repetition rate). Solution samples were contained in 1 mm quartz cuvettes and the emission signal was acquired at a  $90^\circ$  angle relative to the incoming excitation beam. The TCSPC time-resolved signal was deconvoluted from the instrument response function (IRF 0.77 ns) by using the following relation (Eq. S1):

$$f(t) = - \left[ y_0 + \sqrt{\frac{\pi}{2}} \cdot \frac{h \cdot \sigma}{\tau} \cdot \exp \left\{ \frac{1}{2} \cdot \left( \frac{\sigma}{\tau} \right)^2 - \frac{t-t_0}{\tau} \right\} \cdot \text{erf} \left\{ \frac{1}{1.41421} \cdot \left( \frac{\sigma}{\tau} - \frac{t-t_0}{\sigma} \right) \right\} \right] \quad (\text{S1})$$

where  $h$  is the amplitude of the Gaussian IRF,  $\sigma$  is the FWHM / 2.35482,  $\tau$  is the fluorescence lifetime, and  $t_0$  is time zero at the center of the Gaussian.

Ultrafast time-resolved fluorescence measurements of spiro-OMeTAD solutions and thin films were conducted using a broadband fluorescence up-conversion instrument (FLUPS, LIOP-TEC). The sample was excited by a 400 nm light pulse produced by frequency doubling of a chirped pulse-amplified (CPA) Ti:sapphire laser output (Libra-HE USP, Coherent, 50 fs pulse length, repetition rate 1 kHz). The fluorescence from the sample was then upconverted by sum-frequency generation with a gate pulse ( $\lambda_g = 1300$  nm) in a BBO crystal (100  $\mu\text{m}$ -thick, Eksma Optics). The gate pulse was produced by a non-linear optical parametric amplifier of the white light continuum (OPerA Solo, Coherent), pumped by the fundamental output of the Ti:sapphire laser. The up-converted signal went through a Czerny-Turner spectrograph, and the full spectrum was finally detected by a CCD camera (Newton 920, Andor). The time correction for the instrument response function (IRF) was calculated using the cross-correlation between the unabsorbed pump and the probe and was 150 fs. An emission slice at 1 ps time delay was taken before and after each measurement to ensure that the sample was stable during the experiment time.

Transient absorption (TA) spectra were measured using a femtosecond pump-probe spectrometer based on a CPA Ti:sapphire laser (CPA-2001, Clark MXR) delivering pulses at  $\lambda = 778$  nm with a pulse width of 150 fs and a repetition rate of 1 kHz. The pump beam consisted of the second harmonic of the fundamental output of the laser ( $\lambda_{\text{exc}} = 389$  nm), generated by passing the beam through a BBO crystal. The probe, consisting of a broadband white light continuum, was produced by passing part of the fundamental through a 5 mm thick oscillating  $\text{CaF}_2$  window. The pump and probe beams were set at magic angle polarization and spatially and temporally overlapped. A chopper, set at 500 Hz, was used to modulate the repetition rate of the pump pulses thus enabling the absorption with and without the pump to be acquired in the same measurement. The probe beam was split into two, with one going to the signal camera and the other to the reference to account for shot-to-shot fluctuations. The signal and reference beams were dispersed by two different grating spectrographs (SpectraPro 2500i, Princeton Instruments) and the transient spectra were detected by respective CCD cameras (S07030-0906, Hamamatsu). The concentration of solutions for TCSPC, FLUPS and TA was  $5.90 \times 10^{-2}$  M spiro-OMeTAD in CB. Molar ratios of spiro / tBP /  $\text{Li}^+$ ,  $\text{Y}^{3+}$  and  $\text{La}^{3+}$  were 1/3.34/0.54, 0.18 and 0.18, respectively. For film samples, the solutions were spin-coated on quartz glass.

Depth profiling of PSCs was analyzed by time-of-flight secondary ion mass spectrometry (ToF-SIMS) using TOF-SIMS-5 instrument (ION-TOF) equipped with a 25 keV bismuth (Bi) primary ion source and a 1 keV  $\text{O}_2$  sputter ion gun which were arranged at an angle of  $45^\circ$  to sample surface.  $150 \times 150 \mu\text{m}^2$  of area were sputtered (with 190 nA  $\text{O}_2^+$  sputter ion) and middle  $40 \times 40 \mu\text{m}^2$  of area were analyzed (with 1 pA of  $\text{Bi}^{3+}$  primary ion beam).

H-NMR spectra were recorded on a Unity Inova 500 NB High-Resolution NMR Console (500 MHz). Chemical shifts were given in ppm using the TMS signal as a reference.

The molecular structure of metal-tBP complexes was calculated using density functional theory (B3LYP/6-31G\* & LANL2DZ>Kr) in a vacuum. The calculations were carried out by using the Spartan 20' v1.0.0 (Wavefunction) program.

Differential scanning calorimetry (DSC) was carried out using a Seiko Exstar 6000 (DSC6100) under an N<sub>2</sub> atmosphere at a heating rate of 10 °C/min. For sampling for DSC measurements, the spiro-OMeTAD powder was obtained by scraping out the spiro-OMeTAD film from the glass substrate, which was dried at 8.0×10<sup>-7</sup> torr for 48 h.

Steady-state photoluminescence (PL) and time-resolved photoluminescence (TRPL) were measured by a Quantaaurus-Tau compact fluorescence lifetime spectrometer (Quantaaurus-Tau C11367-12, Hamamatsu). The film samples were excited with 464 nm laser (PLP-10, model M12488-33, peak power of 231 mW and pulse duration of 53 ps, Hamamatsu) pulsed at a repetition frequency of 10 MHz for steady-state PL and 1 MHz for TRPL.

Ultraviolet photoelectron spectroscopy (UPS) measurements were carried out on ESCALAB 250 XPS system (Thermo Fisher Scientific) with He I (21.2 eV).

FT-IR spectra were collected within the wave numbers region (600 - 4000 cm<sup>-1</sup>) using Bruker IFS-66/S (SENSOR27) Samples for FT-IR were prepared by dissolving metal-TFSI powder in tBP (metal ion : tBP = 1:8, molar ratio).

The external quantum efficiency (EQE) spectra were collected by using Quant-300 quantum efficiency system (Newport) in which a monochromatic beam was generated from a 100 W Xenon source lamp. Transient photo voltage (TPV) and current (TPC) was measured with 470 nm monochromatic beam (with 5 ms pulse width) coupled with digital oscilloscope.

Current density-voltage (*J-V*) curves were measured (reverse and forward scan direction with a scan rate of 130 mV/s) under AM 1.5G one sun (100 mW cm<sup>-2</sup>) illumination using a solar simulator (Oriel Sol 3A, class AAA) equipped with 450 W Xenon lamp (Newport 6280NS) and a Keithley 2400 source meter. The light intensity was adjusted by an NREL-calibrated Si solar cell having KG-5 filter. The device was covered with a metal mask with an aperture area of 0.10 cm<sup>2</sup>. The illumination stability test was conducted with a white LED (100 mW cm<sup>-2</sup>) in the N<sub>2</sub> glove box. The temperature of devices was maintained 19~20 °C by a temperature-controlled Al plate with four Peltier devices and a cooling module (15-18 °C, homemade setup). To find the voltage at maximum power point (*V*<sub>MAX</sub>) for maximum power point tracking (MPPT) and stabilized PCE, *J-V* curves were measured (with a scan rate of 130 mV/s) at every 24 h from 0 h to 528 h and every 48 h from 528 h to 1008 h in N<sub>2</sub> at room temperature using a solar simulator (VeraSol-2 LED Class AAA Solar Simulator (Newport), 100 mW cm<sup>-2</sup>). *V*<sub>MAX</sub> was determined from the average value of *V*<sub>MAXS</sub> obtained from reverse and forward scans. To check the stabilized PCE, *J-t* curves were measured with applied *V*<sub>MAX</sub> for 500 s after each *J-V* measurement. To track the maximum power point, all devices were transferred to the N<sub>2</sub>-filled glove box and *V*<sub>MAX</sub> was applied under white LED (100 mW cm<sup>-2</sup>).

For the thermal stability test, devices were stored on a hot plate (AS ONE, ND-1A) at 85 °C in an N<sub>2</sub>-filled glove box and covered with a dark glass container. *J-V* curves were measured after 24 h, 96 h, 192 h, 432 h, 672 h and 1032 h in N<sub>2</sub> using a solar simulator (Oriel Sol 3A, class AAA). All devices were cooled down to room temperature (21~22 °C) before measurement. MPPT measurement at 65 °C was performed by using a sulfur lamp (82 mW cm<sup>-2</sup>) and chamber-type zig (McScience) coupled with PID controlled heater and thermocouple.

## SUPPLEMENTAL INFORMATION

Figures S1–S42, Tables S1–S6 and Note S1–S5

## ACKNOWLEDGMENTS

N.-G.P. and S.-G.K. acknowledge financial support from the National Research Foundation of Korea (NRF) grants funded by the Korean government (MSIT) under contract NRF-2021R1A3B1076723 (Research Leader Program) and NRF-2022M3J1A1085280 (Carbon Neutral Technology Program). J.-E.M. acknowledges financial support by the Swiss National Science Foundation (SNF, grant no. 200021\_175729) and the National Center of Competence in Research “Molecular Ultrafast Science and Technology” (NCCR-MUST), a research instrument of the SNF. The work was also partially supported by the U.S. Department of Energy under Contract No. DE-AC36-08GO28308 with Alliance for Sustainable Energy, Limited Liability Company (LLC), the Manager and Operator of the National Renewable Energy Laboratory. S.-G.K. and K.Z. acknowledge the support from the Advanced Perovskite Cells and Modules program of the National Center for Photovoltaics, funded by the U.S. Department of Energy, Office of Energy Efficiency and Renewable Energy, Solar Energy Technologies Office. The views expressed in the article do not necessarily represent the views of the DOE or the U.S. Government.

## AUTHOR CONTRIBUTIONS

M.G., J.-E.M., K.Z. and N.-G.P. supervised this work. S.-G.K., K.Z., M.G., J.-E.M. and N.-G.P. conceived and developed the idea. S.-G.K., G.C.F., E.S., A.T.T. and D.-A.P. performed the experiments and characterization. Writing – original draft: S.-G.K. and J.-E.M. prepared the draft. M.G., J.-E.M., K.Z. and N.-G.P. reviewed and edited the draft. All the authors participated in the discussion of the results.

## DECLARATION OF INTERESTS

The authors declare no competing interests.

## Figure 1. Photo-oxidation of spiro-OMeTAD in the presence of various metal-tBP complexes

(A) Pictures of fresh and white light-exposed spiro-OMeTAD precursor solutions with M<sup>I</sup>-tBP (M<sup>I</sup> = Li<sup>+</sup>, Na<sup>+</sup>, K<sup>+</sup>, Rb<sup>+</sup>, Cs<sup>+</sup>), M<sup>II</sup>-tBP (M<sup>II</sup> = Mg<sup>2+</sup>, Ca<sup>2+</sup>, Sr<sup>2+</sup>, Ba<sup>2+</sup>), and M<sup>III</sup>-tBP (M<sup>III</sup> = Sc<sup>3+</sup>, Y<sup>3+</sup>, La<sup>3+</sup>) added. (B) UV-vis spectra of fresh and light-exposed spiro-OMeTAD precursor solutions

without and with metal-tBP complexes. All solutions in chlorobenzene (CB) were exposed to white light emitted by an LED ( $1 \text{ mW cm}^{-2}$ ) for 30 minutes in an  $\text{N}_2$  glove box (5 ppm of trace  $\text{O}_2$ ,  $\text{H}_2\text{O} < 0.1 \text{ ppm}$ ). The concentration of solutions for UV-vis was  $2.95 \times 10^{-2} \text{ M}$  (spiro-OMeTAD) in CB. The molar ratio of spiro-OMeTAD/tBP/metal ion in metal-TFSI was 1/3.34/0.54 ( $\text{Li}^+ \sim \text{Cs}^+$ ), 0.36 ( $\text{Mg}^{2+} \sim \text{Ba}^{2+}$ ) and 0.18 ( $\text{Sc}^{3+} \sim \text{La}^{3+}$ ).

### Figure 2. Photochemistry of spiro-OMeTAD with $\text{M}^{3+}$ -tBP complex

Emission dynamics of (A) spiro-OMeTAD and (B) spiro-OMeTAD with  $\text{La}(\text{TFSI})_3$  films. Green and red dots represent the absence and presence of tBP, respectively. The fitted curves are shown as solid black lines. Transient absorption (TA) spectra of spiro-OMeTAD film employing (C) tBP only and (D)  $\text{La}^{3+}$ -tBP complex. Decay-associated spectra (DAS) of the spiro-OMeTAD film with (E) tBP only and (F)  $\text{La}^{3+}$ -tBP complex. TA spectra were recorded upon laser pulse excitation ( $\lambda_{\text{exc}} = 389 \text{ nm}$ , pulse duration 200 fs). DAS was obtained from TA spectra by global fitting with bi-exponential function.

### Figure 3. Photoinduced symmetry-breaking charge separation

Energy scheme representing the HOMO and LUMO levels of two adjacent spiro-OMeTAD molecules, noted  $\text{S}_A$  and  $\text{S}_B$ .

### Figure 4. Performance of photo-doped spiro-OMeTAD and PSCs

(A) Steady-state photoluminescence (PL) and (B) time-resolved photoluminescence (TRPL) spectra of glass/perovskite/spiro-OMeTAD devices with photo-doped spiro-OMeTAD films with various metal-tBP complexes, along with  $\text{Li}^+$ -tBP-based air-oxidized spiro-OMeTAD one. (C) Energy level diagram of perovskite ( $\text{FA}_{0.92}\text{Cs}_{0.08}\text{PbBr}_{0.15}\text{I}_{2.85}$ ) and spiro-OMeTAD aged in dry air with  $\text{Li}^+$ -tBP and photo-doped with  $\text{Y}^{3+}$ - and  $\text{La}^{3+}$ -tBP complexes. Current density ( $J$ )-voltage ( $V$ ) curves of PSCs employing (D)  $\text{Li}^+$ -based air-oxidized spiro-OMeTAD and (E)  $\text{Y}^{3+}$ - and (F)  $\text{La}^{3+}$ -based photo-doped spiro-OMeTAD. The device structure was FTO/QD- $\text{SnO}_2$ /Perovskite/spiro-OMeTAD/Ag and an AR-coated high transparent FTO was used.

### Figure 5. Operational stability of PSCs.

Time-of-flight secondary ion mass spectrometry (ToF-SIMS) ( $\text{Li}^+$ ,  $\text{Y}^+$ ,  $\text{La}^+$ ,  $\text{Cs}^+$ ,  $\text{Pb}^+$ ,  $\text{Sn}^+$ , and  $\text{Au}^+$ ) of the unencapsulated devices with (A)  $\text{Li}^+$ -tBP-based air-oxidized spiro-OMeTAD, (B)  $\text{Y}^{3+}$ -tBP-based photo-doped spiro-OMeTAD and (C)  $\text{La}^{3+}$ -tBP-based photo-doped spiro-OMeTAD before (solid lines) and after 1008 hour-illumination (dashed lines). (D) Time-evolution of normalized PCEs (stabilized) from the three types of devices under illumination from 0 to 1008 hours. For  $\text{Li}^+$ -tBP-based spiro-OMeTAD, PSCs were aged in dry air for 72 h (best performance condition). Measurement conditions: MPPT, LED lamp with  $100 \text{ mW cm}^{-2}$ ,  $19 \sim 20 \text{ }^\circ\text{C}$ , and  $\text{N}_2$  atmosphere (5 ppm of trace  $\text{O}_2$ ,  $\text{H}_2\text{O} < 0.1 \text{ ppm}$ ).

## REFERENCES\*

1. Kim, H.-S., Lee, C.-R., Im, J.-H., Lee, K.-B., Moehl, T., Marchioro, A., Moon, S.-J., Humphry-Baker, R., Yum, J.-H., Moser, J.-E., et al. (2012). Lead Iodide Perovskite Sensitized All Solid-State Submicron Thin Film Mesoscopic Solar Cell with Efficiency Exceeding 9%. *Sci. Rep.* *2*, 591. <https://doi.org/10.1038/srep00591>
2. Lee, M. M., Teuscher, J., Miyasaka, T., Murakami, T. N., Snaith, H. J. (2012). Efficient Hybrid Solar Cells Based on Meso-Superstructured Organometal Halide Perovskites. *Science* *338*, 643–647. <https://doi.org/10.1126/science.1228604>
3. NREL. *Best Research-Cell Efficiency Chart*. <https://www.nrel.gov/pv/cell-efficiency.html> (accessed April 30, 2023.)
4. Hawash, Z., Ono, L. K., Qi, Y. (2016). Moisture and Oxygen Enhance Conductivity of LiTFSI-Doped Spiro-MeOTAD Hole Transport Layer in Perovskite Solar Cells. *Adv. Mater. Interfaces* *3*, 1600117. <https://doi.org/10.1002/admi.201600117>
5. Cappel, U. B., Daeneke, T., Bach, U. (2017). Oxygen-Induced Doping of Spiro-MeOTAD in Solid-State Dye-Sensitized Solar Cells and Its Impact on Device Performance. *Nano Lett.* *12*, 4925–4931. <https://doi.org/10.1021/nl302509q>
6. Wang, S., Yuan, W., Meng, Y. S. (2013). Spectrum-Dependent Spiro-OMeTAD Oxidization Mechanism in Perovskite Solar Cells. *ACS Appl. Mater. Interfaces* *7*, 24791–24798. <https://doi.org/10.1021/acsami.5b07703>
7. Liu, X., Zheng, B., Shi, L., Zhou, S., Xu, Z., Liu, Z., Yun, J. S., Choi, E., Zhang, M., Lv, Y., et al. (2023). Perovskite solar cells based on spiro-OMeTAD stabilized with an alkylthiol additive. *Nat. Photon* *17*, 96–105. <https://doi.org/10.1038/s41566-022-01111-x>
8. Svanström, S., Jacobsson, T. J., Boschloo, G., Johansson, E. M. J., Rensmo, H., Cappel, U. B. (2020). Degradation Mechanism of Silver Metal Deposited on Lead Halide Perovskites. *ACS Appl. Mater. Interfaces* *12*, 7212–7221. <https://doi.org/10.1021/acsami.9b20315>
9. Huang, J., Tan, S., Lund, P. D., Zhou, H. (2017). Impact of H<sub>2</sub>O on organic–inorganic hybrid perovskite solar cells. *Energy Environ. Sci.* *10*, 2284–2311. <https://doi.org/10.1039/C7EE01674C>
10. Bryant, D., Aristidou, N., Pont, S., Sanchez-Molina, I., Chotchunangatchaval, T., Wheeler, S., Durrant, J. R., Haque, S. A. (2016). Light and oxygen induced degradation limits the operational stability of methylammonium lead triiodide perovskite solar cells. *Energy Environ. Sci.* *9*, 1655–1660. <https://doi.org/10.1039/C6EE90023B>
11. Senocrate, A., Acartürk, T., Kim G. Y., Merkle, M., Starke, U., Grätzel, M., Maier, J. (2018). Interaction of oxygen with halide perovskites. *J. Mater. Chem. A* *6*, 10847–10855.

<https://doi.org/10.1039/C8TA04537B>

12. Kim, S.-G., Le, T. H., de Monfreid, T., Goubard, F., Bui, T., Park, N.-G. (2021). Capturing Mobile Lithium Ions in a Molecular Hole Transporter Enhances the Thermal Stability of Perovskite Solar Cells. *Adv. Mater.* *33*, 2007431. <https://doi.org/10.1002/adma.202007431>
13. Chen, D.-Y., Tseng, W.-H., Liang, S.-P., Wu, C.-I., Hsu, C.-W., Chi, Y., Hung, W.-Y., Chou, P.-T. (2012). Application of F4TCNQ doped spiro-MeOTAD in high performance solid state dye sensitized solar cells, *Phys. Chem. Chem. Phys.* *14*, 11689–11694. <https://doi.org/10.1039/C2CP41855J>
14. Luo, J., Jia, C., Wan, Z., Han, F., Zhao, B., Wang, R. (2017). The novel dopant for hole-transporting material opens a new processing route to efficiently reduce hysteresis and improve stability of planar perovskite solar cells. *J. Power Sources* *342*, 886–895. <https://doi.org/10.1016/j.jpowsour.2017.01.010>
15. Ye, T., Wang, J., Chen, W., Yang, Y., He, D. (2017). Improved Performance and Reproducibility of Perovskite Solar Cells by Well-Soluble Tris(pentafluorophenyl)borane as a p-Type Dopant, *ACS Appl. Mater. Interfaces* *9*, 17923–17931. <https://doi.org/10.1021/acsami.7b02969>
16. Liu, Q., Fan, L., Zhang, Q., Zhou, A., Wang, B., Bai, H., Tian, Q., Fan, B., Zhang, T. (2017) Benzoyl Peroxide as an Efficient Dopant for Spiro-OMeTAD in Perovskite Solar Cells. *ChemSusChem* *10*, 3098–3104. <https://doi.org/10.1002/cssc.201700872>
17. Tan, B., Raga, S. R., Chesman, A. S. R., Furer, S. O., Zheng, F., McMeekin, D. P., Jiang, L., Mao, W., Lin, X., Wen, X., et al. (2019). LiTFSI-Free Spiro-OMeTAD-Based Perovskite Solar Cells with Power Conversion Efficiencies Exceeding 19%. *Adv. Energy Mater.* *9*, 1901519. <https://doi.org/10.1002/aenm.201901519>
18. Zhang, T., Wang, F., Kim, H.-B., Choi, I.-W., Wang, C., Cho, E., Konefal, R., Puttisong, Y., Terado, K., Kobera, L., et al. (2022), Ion-modulated radical doping of spiro-OMeTAD for more efficient and stable perovskite solar cells. *Science* *377*, 495–501. <https://doi.org/10.1126/science.abo2757>
19. Seo, J.-Y., Akin, S., Zalibera, M., Ruiz Preciado, M. A., Kim, H.-S., Zakeeruddin, S. M., Millić, J. V., Grätzel, M. (2021). Dopant engineering for spiro-OMeTAD hole-transporting materials towards efficient perovskite solar cells. *Adv. Funct. Mater.* *31*, 2102124. <https://doi.org/10.1002/adfm.202102124>
20. Noh, J. H., Jeon, N. J., Choi, Y. C., Nazeeruddin, Md. K., Grätzel, M., Seok, S. I. (2013). Nanostructured TiO<sub>2</sub>/CH<sub>3</sub>NH<sub>3</sub>PbI<sub>3</sub> heterojunction solar cells employing spiro-OMeTAD/Co-complex as hole-transporting material. *J. Mater. Chem. A* *1*, 11842–11847. <https://doi.org/10.1039/C3TA12681A>

21. Pham, N. D., Shang, J., Yang, Y., Hoang, M. T., Tiong, V. T., Wang, Fan, X., L., Chen, P., Kou, L., Wang, et al. (2020). Alkaline-earth bis(trifluoromethanesulfonimide) additives for efficient and stable perovskite solar cells. *Nano Energy* 69, 104412. <https://doi.org/10.1016/j.nanoen.2019.104412>
22. Mohanraj, S. J., Stihl, M., Simon, E., von Sicard, O., Schmidt, G., Fleischer, M., Neuber, C., Thelakkat, M. (2019). Li-Salt-Free, Coevaporated Cu(TFSI)<sub>2</sub>-Doped Hole Conductors for Efficient CH<sub>3</sub>NH<sub>3</sub>PbI<sub>3</sub> Perovskite Solar Cells. *ACS Appl. Energy Mater.* 2, 3469–3478. <https://doi.org/10.1021/acsaem.9b00260>
23. Pellaroque, S. A., Noel, N. K., Habisreutinger, S. N., Zhang, Y., Barlow, S., Marder, S. R., Snaith, H. J. (2017). Efficient and Stable Perovskite Solar Cells Using Molybdenum Tris(dithiolene)s as p-Dopants for Spiro-OMeTAD. *ACS Energy Lett.* 2, 2044–2050. <https://doi.org/10.1021/acsenergylett.7b00614>
24. Seo, J.-Y., Kim, H.-S., Akin, S., Stojanovic, M., Simon, E., Fleischer, M., Hagfeldt, A., Zakeeruddin, S. M., Grätzel, M. (2018). Novel p-dopant toward highly efficient and stable perovskite solar cells, *Energy Environ. Sci.* 11, 2985–2992. <https://doi.org/10.1039/C8EE01500G>
25. Saygili, S. Y., Kim, H.-S., Yang, B., Suo, J., Muñoz-Garcia, A. B., Pavone, M., Hagfeldt, A. (2020). Revealing the Mechanism of Doping of spiro-MeOTAD via Zn Complexation in the Absence of Oxygen and Light. *ACS Energy Lett.* 5, 1271–1277. <https://doi.org/10.1021/acsenergylett.0c00319>
26. Nguyen, S. W. H., Bailie, C. D., Unger, E. L., McGehee, M. D. (2014). Enhancing the hole-conductivity of spiro-OMeTAD without oxygen or lithium salts by using spiro(TFSI)<sub>2</sub> in perovskite and dye-sensitized solar cells. *J. Am. Chem. Soc.* 136, 10996–11011. <https://doi.org/10.1021/ja504539w>
27. Wang, S., Yuan, W., Meng, Y. S. (2015). Spectrum-Dependent Spiro-OMeTAD Oxidization Mechanism in Perovskite Solar Cells. *ACS Appl. Mater. Interfaces* 7, 24791–24798. <https://doi.org/10.1021/acsami.5b07703>
28. Vale, B. R. C., Socie, E., Burgos-Caminal, A., Bettini, J., Schiavon, M. A., Moser, J.-E. (2020). Exciton, biexciton, and hot exciton dynamics in CsPbBr<sub>3</sub> colloidal nanoplatelets. *J. Phys. Chem. Lett.* 11, 387–394. <https://doi.org/10.1021/acs.jpcllett.9b03282>
29. Ramirez, S. C. E., Chen, S., Powers-Riggs, N. E., Schlesinger, I., Young, R. M., Wasielewski, M. R. (2020). Symmetry-breaking charge separation in the solid state: Tetra(phenoxy)perylene diimide polycrystalline films. *J. Am. Chem. Soc.* 142, 18243–18250. <https://doi.org/10.1021/jacs.0c09185>
30. Fish, S. G., Moreno-Naranjo, J. M., Billion, A., Kratzert, D., Hack, E., Krossing, I., Nüesch, F., Moser, J.-E. (2021). Critical role of H-aggregation for high-

efficiency photoinduced charge generation in pristine pentamethine cyanine salts. *Phys. Chem. Chem. Phys.* **23**, 23886–23895.

<https://doi.org/10.1039/D1CP03251H>

31. Liu, M., Dahlström, S., Ahläng, C., Wilken, S., Degtarev, A., Matuhina, A., Hadadian, M., Markkanen, M., Aitola, K., Kamppinen, A., et al. (2022). Beyond hydrophobicity: how F4-TCNQ doping of the hole transport material improves stability of mesoporous triple-cation perovskite solar cells. *J. Mater. Chem. A* **10**, 11721–11731. <https://doi.org/10.1039/D2TA02588D>
32. Wang, X., Wu, J., Yang, Y., Liu, X., Guo, Q., Song, Z., Li, G., Lan, Z., Huang, M. (2019). High performance and stable perovskite solar cells using vanadic oxide as a dopant for spiro-OMeTAD. *J. Mater. Chem. A* **7**, 13256–13264. <https://doi.org/10.1039/C9TA03351C>
33. Stolterfoht, S M., Caprioglio. P., Wolff, C. M., Márquez, J. A., Nordmann, J., Zhang, S., Rothhardt, D., Hörmann, U., Amir, Y., Redinger, A., et al. (2019). The impact of energy alignment and interfacial recombination on the internal and external open-circuit voltage of perovskite solar cells. *Energy Environ. Sci.* **12**, 2778–2788. <https://doi.org/10.1039/C9EE02020A>
34. Caprioglio, S P., Stolterfoht, M., Wolff, C. M., Unold, T., Rechm B., Albrecht, S., Neher, D. (2019). On the Relation between the Open-Circuit Voltage and Quasi-Fermi Level Splitting in Efficient Perovskite Solar Cells. *Adv. Energy Mater.* **9**, 1901631. <https://doi.org/10.1002/aenm.201901631>
35. Domanski, S K., Alharbi, E. A., Hagfeldt, A., Grätzel, M., Tress, W. (2018). Systematic investigation of the impact of operation conditions on the degradation behaviour of perovskite solar cells. *Nat. Energy* **3**, 61–67. <https://doi.org/10.1038/s41560-017-0060-5>
36. Saliba, S M., Stolterfoht, M., Wolff, C. M., Neher, D., Abate, A. (2018). Measuring Aging Stability of Perovskite Solar Cells. *Joule* **2**, 1019–1027. <https://doi.org/10.1016/j.joule.2018.05.005>
37. Domanski, K., Roose, B., Matsui, T., Saliba, M., Turren-Cruz, S.-H., Correa-Baena, J.-P., Carmona, C. R., Richardson, G., Foster, J. M., Angelis, F. D., et al. (2017). Migration of cations induces reversible performance losses over day/night cycling in perovskite solar cells. *Energy Environ. Sci.* **10**, 604–613. <https://doi.org/10.1039/C6EE03352K>
38. Kim, S.-G., Li, C., Guerrero, A., Yang, J.-M., Zhong, Y., Bisquert, J., Huettner, S., Park, N.-G. (2019). Potassium ions as a kinetic controller in ionic double layers for hysteresis-free perovskite solar cells. *J. Mater. Chem. A* **7**, 18807–18815. <https://doi.org/10.1039/C9TA07595J>
39. Li, Z., Xiao, C., Yang, Y., Harvey, S. P., Kim, D. H., Christians, J. A., Yang, M., Schulz, P., Nanayakkara, S. U., Jiang, C.-S., et al. (2017). Extrinsic ion migration in perovskite solar cells.

Energy Environ. Sci. *10*, 1234–1242.

<https://doi.org/10.1039/C7EE00358G>

40. Ding, S C., Yin, L., Wang, J., Larini, V., Zhang, L., Huang, R., Nyman, M., Zhao, L., Zhao, C., Li, W, et al. (2023). Boosting Perovskite Solar Cells Efficiency and Stability: Interfacial Passivation of Crosslinked Fullerene Eliminates the “Burn-in” Decay. *Adv. Mater.* *35*, 2207656.

<https://doi.org/10.1002/adma.202207656>

41. Lin, Y., Chen, B., Fang, Y., Zhao, J., Bao, C., Yu, Z., Deng, Y., Rudd, P. N., Yan, Y., Yuan, Y., et al.

(2018). Excess charge-carrier induced instability of hybrid perovskites. *Nat Commun.* *9*, 4981.

<https://doi.org/10.1038/s41467-018-07438-w>

42. Son, D.-Y., Kim, S.-G., Seo, J.-Y., Lee, S.-H., Shin, H., Lee, D., Park, N.-G. (2018). Universal Approach toward Hysteresis-Free Perovskite Solar Cell via Defect Engineering. *J. Am. Chem. Soc.* *140*, 1358–1364.

<https://doi.org/10.1021/jacs.7b10430>

43. Dawson. J. A., Naylor. A. J., Eames, C., Roberts, M., Zhang, W., Snaith, H. J., Bruce, P. G., Islam, M. S. (2017).

Mechanisms of Lithium Intercalation and Conversion Processes in Organic–Inorganic Halide Perovskites. *ACS Energy Lett.* *2*, 1818–1824.

<https://doi.org/10.1021/acsenergylett.7b00437>

44. Khenkin, M. V., Katz, E. A., Abate, A., Bardizza, G., Berry, J. J., Brabec, C., Brunetti, F., Bulović, V., Burlingame, Q., Carlo, A. D., et al. (2020). Consensus statement for stability assessment and reporting for perovskite photovoltaics based on ISOS procedures. *Nat. Energy* *5*, 35–49.

<https://doi.org/10.1038/s41560-019-0529-5>

<https://doi.org/10.1038/s41560-019-0529-5>